ELSEVIER

Lattice dynamical finite-element method

Xiaohui Liu [a], Jianfeng Gu [a,*], Yao Shen [a], Ju Li [b,*], Changfeng Chen [c]

[a] *Shanghai Key Laboratory of Materials Laser Processing and Modification, School of Materials Science and Engineering, Shanghai Jiao Tong University, Shanghai 200240, China*
[b] *Department of Materials Science and Engineering, University of Pennsylvania, Philadelphia, PA 19104, USA*
[c] *Department of Physics and High Pressure Science and Engineering Center, University of Nevada, Las Vegas, NV 89154, USA*

Abstract

A lattice dynamical finite-element method (LDFEM) is proposed for multiscale analysis of stressed complex crystals. Interatomic potential is embedded into the constitutive relation within the hyperelasticity framework, and two energy-based lattice instability criteria, the Λ criterion and the soft phonon criterion, are incorporated into LDFEM for capturing stress-driven instabilities in a perfect crystal. The simulations of uniaxial loadings and a two-dimensional nanoindentation of B2-NiAl are performed using both LDFEM and molecular dynamics (MD). The good agreement of the simulated mechanical responses between the two methods validates the proposed method. Combination of the two criteria can provide a powerful tool for predicting lattice instabilities in complex crystals under load at zero or low temperatures.
© 2009 Acta Materialia Inc. Published by Elsevier Ltd. All rights reserved.

1. Introduction

Multiscale simulations have been widely used for the investigation of material response that involves different length scales. Compared with atomistic simulation approaches such as molecular dynamics (MD) and ab initio methods, multiscale methods are more efficient for studying large-length-scale systems while capturing critical features at atomic scale. Generally speaking, multiscale methods can be classified into two types: concurrent and hierarchical methods [1]. Concurrent multiscale methods couple different length scales in each sub-domain and perform simulations in each scale simultaneously. As a typical concurrent multiscale method, the local–nonlocal combination version of the quasicontinuum (QC) method proposed by Tadmor et al. [2] incorporates continuum theories with atomistic

models, and reduces the degrees of freedom and computational demand by finite-element method (FEM) without losing atomistic details in regions of interest [3]. It has been used for investigating nanoindentation [4–11], fracture [12–14], grain boundaries [11,15–18] and dislocations [2–20]. Other concurrent multiscale methods include the macroscopic-atomistic-ab initio dynamics (MAAD) proposed by Abraham et al. [21], the coarse-grained molecular dynamics (CGMD) by Rudd and Broughton [22], the coupled atomistic and discrete dislocation (CADD) model by Shilkrot et al. [23], and coupling molecular dynamics with continuum mechanics via a bridging domain by Belytschko and Xiao [24]. Hierarchical multiscale methods, on the other hand, employ a continuum approximation to model subscale systems via a homogenization procedure and solve problems in the continuum framework. It includes the local QC [25–31] and some other methods with a similar concept of the local QC, such as the work of employing a mixed atomistic/continuum technique to solve boundary value problems in strained semiconductors by Johnson et al. [32], the local formulation implemented to study the behavior of carbon

* Corresponding authors. Tel.: +86 021 34203743; fax: +81 021 34203742.
E-mail addresses: gujf@sjtu.edu.cn (J. Gu), liju@seas.upenn.edu (J. Li).

nanotubes (CNT) by Zhang et al. [33], and the interatomic potential finite-element model (IPFEM) embedded with a lattice instability criterion for predicting homogenous instability in perfect crystals proposed by Li et al. [34].

As an important off-shoot of the local QC, IPFEM offers an efficient and accurate tool for multiscale analysis at zero temperature. It employs the Cauchy–Born (CB) hypothesis [35], linking the macro elastic deformation and the atomic motions, to formulate the constitutive law based on empirical interatomic potentials within the framework of hyperelasticity. Li et al. [34] first studied the nanoindentation of Cu by IPFEM, and as its extensions, Van Vliet et al. [36] performed a study of quantifying the early stage of plasticity in fcc metals, Zhu et al. [37] presented a predictive model of nanoindentation-induced homogeneous dislocation in Cu, and Zhong et al. [38] simulated nanoindentation and predicted dislocation in three single crystals of Al, Cu and Ni. In our previous study [39], the anisotropy in homogeneous dislocation nucleation by nanoindentation of single-crystal Cu has also been investigated by IPFEM. However, all of these investigations above focused on monatomic single crystals which contain only one atom per primitive unit cell. It would be interesting to study more complex crystals, because such lattices with multiple atoms per primitive unit cell like Si [21,25–27,31,32], CNT [24,33] and compounds [28,30] may exhibit more sophisticated mechanical responses under loadings. A related pioneering work by Tadmor et al. [25] presented the constitutive relations using atomistic energy functionals for complex crystals based on the local QC.

An important work in IPFEM is to identify homogenous lattice instability such as dislocation, twin, microcrack and phase transformation with instability criteria. Most of the monatomic crystals exhibit elastic instability under critical loading conditions, therefore Refs. [36–39] based on IPFEM predicted homogenous lattice instability with the Λ criterion proposed by Li [34] or its equivalent criterion, which can capture elastic instability effectively. However, for complex crystals or even simple lattices like Al under simple loadings [40] at zero or low finite temperatures, the homogeneous lattice instability is usually a dynamical instability occurring firstly with a wave number away from the center of the Brillouin zone, rather than an elastic instability corresponding to the long wavelength limit. Thus, the more general soft phonon instability criterion is of great significance to be embedded into IPFEM simulations of mechanical behavior of materials, especially for complex crystals.

In the present study, we propose a lattice dynamical finite-element method (LDFEM) as an extension of IPFEM to study more complex Bravais crystals based on the embedded-atom method (EAM) potential [41], and predict homogenous lattice instability by both the Λ criterion and the soft phonon criterion. The rest of the paper is organized as follows. Section 2 briefly describes the continuum formulation under finite elastic deformation, followed by presenting the constitutive relation based on the EAM potential for complex crystals in Section 3, and reviewing the two instability criteria in Section 4. Section 5 gives three examples of the LDFEM's application including uniaxial loadings and a two-dimensional (2-D) indentation of single-crystal B2-NiAl, and compares the results with those by MD simulations. Section 6 presents the conclusions and discussions.

2. Continuum formulation under finite elastic deformation

Consider a reference configuration of a material occupying domain Ω_0. When the material undergoes a uniform deformation, the material coordinate $\mathbf{X}$ in the reference configuration is mapped to $\mathbf{x}$ in the current (or deformed) configuration occupying domain Ω, given by [42]

$$\mathbf{x} = \mathbf{X} + \mathbf{u}(\mathbf{X}), \tag{1}$$

$$\mathbf{F} = \frac{\partial \mathbf{x}}{\partial \mathbf{X}} = \mathbf{I} + \frac{\partial \mathbf{u}}{\partial \mathbf{X}}, \tag{2}$$

where $\mathbf{u}(\mathbf{X})$ is the displacement vector from $\mathbf{X}$ to $\mathbf{x}$, $\mathbf{F}$ is the deformation gradient, and $\mathbf{I}$ is the identity tensor. Without considering the body force, the equilibrium equation in the reference configuration can be described by

$$\nabla \cdot \mathbf{P} = \mathbf{0} \text{ in } \Omega_0, \tag{3}$$

and the boundary conditions are given by

$$\mathbf{u} = \bar{\mathbf{u}} \quad \text{on } \Gamma_u, \tag{4}$$

$$\mathbf{P} \cdot \mathbf{n} = \bar{\mathbf{T}} \quad \text{on } \Gamma_t, \tag{5}$$

where $\mathbf{P}$ is the nominal stress tensor, $\bar{\mathbf{u}}$ is the prescribed displacement vector on the boundary Γ_u, and $\bar{\mathbf{T}}$ is the surface traction vector per unit undeformed area on the boundary Γ_t. $\mathbf{P}$ is given by $\mathbf{SF}^T$, where $\mathbf{S}$ is the second Piola–Kirchhoff stress tensor. As is known, if the external work applied to a material is independent of loading history, the constitutive law can be described as the hyperelastic formulation,

$$\mathbf{S} = \frac{\partial W}{\partial \mathbf{E}}, \tag{6}$$

$$\mathbf{C} = \frac{\partial \mathbf{S}}{\partial \mathbf{E}} = \frac{\partial^2 W}{\partial \mathbf{E} \partial \mathbf{E}}, \tag{7}$$

where W is the strain energy density, $\mathbf{E}$ is the Green strain tensor, given by $\mathbf{E} = \frac{1}{2}(\mathbf{F}^T \mathbf{F} - \mathbf{I})$, and $\mathbf{C}$ is the second elastic tensor. Eqs. (3)–(7) provide a Lagrangian description of solid elastic deformation at the continuum level. How to establish the connection between the macro elastic deformation and the micro atomic motions is the key to realizing a multiscale simulation combining the intrinsic advantages of simulation techniques at different length scales.

3. Constitutive relation of LDFEM based on the EAM potential for complex crystals

In order to embed the atomistic interactions governing the mechanical response into the constitutive relation for

continuum, the linkage between atomic movements and the continuum deformation should be established. It can be implemented through the CB hypothesis, which states that an undeformed Bravais lattice vector of a crystal in the reference configuration can be mapped into a deformed lattice vector in the current configuration, according to the deformation gradient $\mathbf{F}$. This hypothesis has been widely employed for multiscale simulations of monatomic crystals. Next, we employ it to formulate the constitutive relation for complex Bravais lattices.

We assume a crystal lattice contains N basis atoms in a primitive unit cell and index each atom as $\alpha = (A, a)$ (or $\beta = (B, b)$, $\gamma = (C, c)$, ...), where A (or B, C, ...) is the primitive unit cell number, and a (or b, c, ...) is the basis atom number. The coordinates of atom α in the reference configuration are given by

$$\mathbf{X}^\alpha = \mathbf{X}^A + \mathbf{Z}^a, a = 1, \ldots N, \tag{8}$$

where $\mathbf{X}^A$ are the coordinates of the atom that occupies the origin basis site (called origin atom) in cell A, and $\mathbf{Z}^a$ are the coordinates of atom α relative to the origin atom. We set $\mathbf{Z}^1 = 0$, so atom $(A, 1)$ (or $(B, 1)$, $(C, 1)$...) represents the origin atom in cell A (or B, C, ...). In a homogenously deformed lattice with a deformation gradient $\mathbf{F}$, the new coordinates of atom α in the deformed configuration can be written as

$$\mathbf{x}^\alpha = \mathbf{F}\mathbf{X}^A + \mathbf{z}^a, \tag{9}$$

where $\mathbf{z}^a$ are the inner displacements of atom α, which are not equal to $\mathbf{F}\mathbf{Z}^a$ in general. The relative position vectors between atoms α and β in the reference and deformed configurations are denoted as $\mathbf{R}^{\alpha\beta}$ and $\mathbf{r}^{\alpha\beta}$, respectively, given by

$$\mathbf{R}^{\alpha\beta} = \mathbf{X}^\beta - \mathbf{X}^\alpha = (\mathbf{X}^B - \mathbf{X}^A) + (\mathbf{Z}^b - \mathbf{Z}^a), \tag{10}$$

$$\mathbf{r}^{\alpha\beta} = \mathbf{x}^\beta - \mathbf{x}^\alpha = \mathbf{F}(\mathbf{X}^B - \mathbf{X}^A) + (\mathbf{z}^b - \mathbf{z}^a) = \mathbf{F}\mathbf{R}^{\alpha\beta} + (\mathbf{z}^b - \mathbf{z}^a). \tag{11}$$

The magnitude of the vector $\mathbf{r}^{\alpha\beta}$ is denoted as $r^{\alpha\beta}$.

The temperature is assumed to be 0 K to exclude the effect of thermal fluctuation of atoms, and the strain energy density W is simply the interatomic potential per unit volume in the reference configuration. Based on the EAM potential, W is given by

$$W = \frac{1}{\Omega_0} \sum_\alpha^\wedge \Psi^\alpha = \frac{1}{\Omega_0} \sum_\alpha^\wedge \left[\sum_{\beta \neq \alpha} \frac{1}{2} V^{\alpha\beta}(r^{\alpha\beta}) + U^\alpha(\bar{\rho}^\alpha) \right], \tag{12}$$

where Ω_0 is the volume of a primitive unit cell in the reference configuration, Ψ^α is the energy of atom α, $V^{\alpha\beta}$ is the pair potential between atoms α and β, U^α is the embedding energy as a function of the host electron density $\bar{\rho}^\alpha$ at the site of atom α, which is given by

$$\bar{\rho}^\alpha = \sum_{\beta \neq \alpha} \rho^\beta(r^{\alpha\beta}), \tag{13}$$

with ρ^β being the electron density function of atom β. The symbol $\sum_\alpha^\wedge$ in Eq. (12) indicates summation only over a

from 1 to N for index α, and the symbol $\sum_{\beta \neq \alpha}$ in Eqs. (12) and (13) indicates that index β runs over all the neighboring atoms around atom α within a specialized cut-off radius R_{cut}.

It is can be seen from Eqs. (11) and (12) that W is dependent on $\mathbf{F}$ and $\mathbf{z}$. For a given $\mathbf{F}$, the inner displacements can be calculated by minimizing the strain energy with respect to $\mathbf{z}$, i.e.,

$$\frac{\partial W}{\partial \mathbf{z}^p} = \frac{\partial W(\mathbf{F}, \mathbf{z})}{\partial \mathbf{z}^p} \bigg|_\mathbf{F} = 0, \ p = 2, \ldots, N. \tag{14}$$

Based on the solved $\mathbf{z}$, the second Piola–Kirchhoff stress $\mathbf{S}$ can be obtained by

$$S_{ij} = \frac{\partial W}{\partial E_{ij}} + \frac{\partial W}{\partial z_m^p} \frac{\partial z_m^p}{\partial E_{ij}}. \tag{15}$$

Substituting Eq. (14) into Eq. (15), we have

$$S_{ij} = \frac{\partial W}{\partial E_{ij}}. \tag{16}$$

The second elastic tensor $\mathbf{C}$ can be computed by differentiating Eq. (15) with respect to $\mathbf{E}$, given by

$$C_{ijkl} = \frac{\partial^2 W}{\partial E_{ij} \partial E_{kl}} + \frac{\partial^2 W}{\partial E_{ij} \partial z_m^p} \frac{\partial z_m^p}{\partial E_{kl}}. \tag{17}$$

The term $\frac{\partial z_m^p}{\partial E_{ij}}$ on the right side of Eq. (17) can be determined by differentiating Eq. (14) with respect to $\mathbf{E}$, i.e.,

$$\frac{\partial^2 W}{\partial E_{ij} \partial z_n^q} + \frac{\partial^2 W}{\partial z_m^p \partial z_n^q} \frac{\partial z_m^p}{\partial E_{ij}} = 0. \tag{18}$$

So

$$\frac{\partial z_m^p}{\partial E_{ij}} = -\left(\frac{\partial^2 W}{\partial z_m^p \partial z_n^q} \right)^{-1} \frac{\partial^2 W}{\partial E_{ij} \partial z_n^q}, \tag{19}$$

Substituting Eq. (19) into Eq. (17), $\mathbf{C}$ can be further rewritten as

$$C_{ijkl} = \frac{\partial^2 W}{\partial E_{ij} \partial E_{kl}} - \left(\frac{\partial^2 W}{\partial z_m^p \partial z_n^q} \right)^{-1} \frac{\partial^2 W}{\partial E_{ij} \partial z_m^p} \frac{\partial^2 W}{\partial E_{ij} \partial z_n^q}. \tag{20}$$

The derivatives of the EAM-based strain energy density W defined in Eq. (12) with respect to $\mathbf{E}$ or/and $\mathbf{z}$ in Eqs. (16) and (20) are given in Appendix A, and the derivatives of r with respect to $\mathbf{E}$ or/and $\mathbf{z}$ are given in Appendix B.

The LDFEM based on the EAM potential for complex Bravais lattices at zero temperature has been formulated as above. The governing Eqs. (3)–(5) can be solved with FEM software package. In our work, it is implemented in ABAQUS/Standard software [43] by writing a user subroutine called UMAT, which needs to provide the Cauchy stress $\boldsymbol{\sigma}$ and the tangent modulus $\mathbf{C}^*$, given by

$$\boldsymbol{\sigma} = \frac{1}{\det(\mathbf{F})} \mathbf{F}\mathbf{S}\mathbf{F}^T, \tag{21}$$

$$\mathbf{C}^* = \frac{\partial^2 W^*}{\partial \mathbf{E}^* \partial \mathbf{E}^*} \bigg|_{\mathbf{E}^*=0}, \tag{22}$$

where the superscript ∗ suggests that the reference configuration is set as the current configuration. In each step, the deformation gradient for each integration point is calculated based on the updated displacement field, and the positions for the neighboring atoms are updated according to the deformation gradient and the inner displacements. If the current configuration is taken as the reference configuration, the Cauchy stress **σ** and the tangent modulus **C**∗ are equivalent to the second Piola–Kirchhoff stress **S** and the second elastic tensor **C**, respectively, which can be obtained by substituting the deformed positions of the neighboring atoms into Eqs. (16) and (20).

4. Lattice instability criteria

4.1. Λ criterion

The Λ criterion proposed by Li et al. [34] originates from the studies of Hill [44,45] and Rice [46]. The former considered that the loss of strong ellipticity of the strain energy density function indicates an elastic instability, and the latter derived the localization of plastic deformation into a shear band as an instability of plastic flow or a precursor to rupture. The Λ criterion considers the Helmholtz free energy change of a representative volume element (RVE) with a homogenous deformation by applying a long elastic plane wave perturbation which gives zero displacements on boundaries. Indeed, the Λ criterion reflects the concavity of the Helmholtz free energy with respect to elastic wave [34,47,48]. The sign of Λ is defined as

$$\Lambda(\mathbf{k}, \mathbf{w}) = \left(C^*_{ijkl} w_i w_k + \sigma_{jl} \right) k_j k_l, \tag{23}$$

where **k** and **w** are normalized vectors defined as the wave vector and the polarization vector, respectively. Once the minimum Λ (Λ_{min}) for a material point becomes non-positive for a given pair of **k** and **w**, a defect will be nucleated. If the corresponding $\mathbf{k}_{min}$ is more perpendicular than parallel to $\mathbf{w}_{min}$, the instability would probably result in a formation of dislocation or twin, with $\mathbf{k}_{min}$ and $\mathbf{w}_{min}$ as its slip plane and Burger vector, respectively. Otherwise, a microcrack is likely nucleated, with $\mathbf{k}_{min}$ and $\mathbf{w}_{min}$ nearly parallel to the crack plane normal. The Λ criterion was applied for the first time to atomic scale in nanoindentation simulation by Li et al. [34], and gave a reliable prediction of dislocation nucleation, which was validated by the MD simulation.

4.2. Soft phonon criterion

Different from the rank-one uniform deformation perturbation applied to a RVE in deriving the Λ criterion, the soft phonon criterion considers a perturbation with respect to relative displacements at atomic scale, which has been employed to investigate the ideal strength of materials [40,49]. As all atomic motions in a crystal with Born–Von Karman periodic boundary conditions (PBCs)

can be viewed as combinations of independent harmonic phonon modes without coupling with each other as a result of no anharmonic effects introduced approximately when temperature approaches zero, the soft phonon criterion gives both necessary and sufficient conditions for structural dynamical instability, i.e., if there exists a phonon mode with an imaginary frequency, the crystal will be unstable, and vice versa. The instability may lead to nucleation of dislocation, crack, modulated structure or new phase, whose structure can be characterized by the soft phonon modes. For instance, the modulation displacements of a newly nucleated modulated structure are summation of harmonics with the soft phonon modes. The frequency and atomic displacements of a soft phonon mode with certain wave vector **q** in the Brillouin zone can be obtained based on analysis of the eigenvalues and eigenvectors of the dynamical matrix [50], defined as

$$\mathbf{D^q}(ab) = \frac{1}{\sqrt{m^a m^b}} \sum_A \Phi \begin{pmatrix} A \\ a \end{pmatrix} \begin{vmatrix} 0 \\ b \end{pmatrix} \exp \left\{ -i\mathbf{q} \cdot \left[\mathbf{x} \begin{pmatrix} A \\ a \end{pmatrix} - \mathbf{x} \begin{pmatrix} 0 \\ b \end{pmatrix} \right] \right\}, \tag{24}$$

where m is the atomic mass, i is the imaginary unit, and Φ is the force constant matrix, given by

$$\Phi(\alpha\beta) = \frac{\partial^2 \bar{\Psi}}{\partial \mathbf{x}^\alpha \partial \mathbf{x}^\beta} - \delta^{\alpha\beta} \sum_\gamma \frac{\partial^2 \bar{\Psi}}{\partial \mathbf{x}^\alpha \partial \mathbf{x}^\gamma}, \tag{25}$$

with $\bar{\Psi}$ being the total potential energy of the system. The expression of the second derivatives of $\bar{\Psi}$ with respect to **x** based on the EAM potential for complex crystals is given in Appendix C.

Note that the soft phonon instability criterion is not tenable rigorously at high temperatures, as the harmonic approximation is no longer rigorous and energies of the modes will be coupled with each other [47], which is, however, not a limitation for the Λ criterion which is based on thermo-elasticity. Both the instability criteria require that the model is under PBCs, or has uniform (or slowly varying) deformation field in which the homogenous unstable region does not contact with external loading directly [47,48]. Generally, the eigenmodes of instability predicted by the Λ criterion correspond to a homogenous deformation at the primitive-cell level, differing from those by the soft phonon analysis which usually indicate an inhomogeneous deformation from one primitive cell to the next. An exceptional case is that a certain phonon mode becomes unstable at the Γ-point in the Brillouin zone, where the soft phonon criterion degenerates to the Λ criterion, i.e., they are equivalent when the dynamical instability occurs in the long wavelength limit.

5. Validation of LDFEM

In this section, we validate the LDFEM simulations of uniaxial loadings and a 2-D cylindrical nanoindentation of single-crystal B2-NiAl with complex Bravais lattices by

comparing the results of the MD simulations implemented with the large-scale atomic/molecular massively parallel simulator (LAMMPS) [51,52]. The EAM potential of NiAl proposed by Mishin [53] is used for both the methods. The LDFEM simulations are performed as static analysis at a temperature of absolute 0 K, in contrast to 0.1 K in the MD simulations, at which the thermal fluctuation of atoms is allowed to activate phonons without introducing too much kinetic energy. The two instability criteria are embedded into the LDFEM simulations to predict homogenous lattice instability, which is characterized by the eigenmodes and compared directly with the MD's visualized images. For simplicity, we just fix the vector **k** in Eq. (23) and the wave vector **q** in Eq. (24) within several low-index and high-symmetry directions, which can cover most instability cases.

It is worth noting that the proposed LDFEM has no inherent length scale, as it originates from the continuum model. However, LDFEM can be assigned the same length scale as that of MD during comparison, which is the basis of the validation of LDFEM by MD.

5.1. Uniaxial loadings

The simulations of the uniaxial tension and compression along the [1 0 0] direction of B2-NiAl single crystal are performed with both LDFEM and MD. As for the LDFEM simulations, a single 8-noded brick element with one reduced integration point and six planes, denoted as x^+, x^-, y^+, y^-, z^+ and z^-, is used to simulate a uniformly deformed cell with each side's original size of unit length. The coordinate system is oriented such that x, y and z axes correspond to the [1 0 0], [0 1 0] and [0 0 1] directions, respectively. The x^-, y^- and z^- planes are fixed in the x, y and z directions, respectively, and the y^+ and z^+ planes are traction free. The x^+ plane is fixed in both the y and z directions, and pulled (or pushed) along the x direction for uniaxial tension (or compression), respectively. In each step, the engineering strain is kept constant of 0.1% (or −0.1%), and the y^+ and z^+ planes are fully relaxed until the engineering stresses of σ_y and σ_z vanish. Note that the six planes of the element do not act as free surfaces of the material but periodic boundaries, as surfaces stress is not considered in the LDFEM's constitutive relation. In the MD simulations, a 3-D periodic cell with 16 primitive unit cells in all the x, y and z directions is used to investigate the uniaxial loading responses. The cell with the same orientations of the brick element in the LDFEM simulations is equilibrated first at a temperature of 0.1 K for 10 ps in the isobaric–isothermal (NPT) ensemble [54] with zero applied pressure, and then deformed by uniaxial tension (or compression) along the x direction at a constant engineering strain rate of 10^{-3} ps^{-1} (or -10^{-3} ps^{-1}) with pressure-free conditions for the other two directions. The calculation of stress includes only the potential portion without kinetic one in order to make comparable to that in the LDFEM computation.

5.1.1. Uniaxial tension

The stress–strain (σ–ε) responses of the uniaxial tension simulated by the two methods are shown in Fig. 1. It can be seen that the σ–ε curves from the LDFEM and MD simulations fit very well before instability. The difference of the curves after instability is due to the fact that the CB hypothesis, the basis of LDFEM, is not true when defects occur in the lattice. LDFEM predicts a dynamical instability at $\varepsilon_x = 9.11\%$ ($\sigma_x = 6.69$ GPa) with the Λ criterion or an elastic instability at $\varepsilon_x = 37.60\%$ ($\sigma_x = 22.72$ GPa) with the soft phonon criterion. The MD simulation validates that the incipient instability under tension is a dynamical instability in essence at $\varepsilon_x = 9.28\%$ ($\sigma_x = 6.78$ GPa), which is in good agreement with the prediction of the soft phonon criterion embedded in the LDFEM. Fig. 2a and b depicts the phonon spectra along high-symmetry directions for the undeformed lattice and the lattice at $\varepsilon_x = 9.11\%$, respectively. It can be seen that one of the acoustic phonon branches has just softened at point M in the Brillouin zone with a wave vector of $\mathbf{q}_1 = \frac{1}{2}\mathbf{a}_1^* + \frac{1}{2}\mathbf{a}_2^* + 0\mathbf{a}_3^*$ (with $\mathbf{q}_1^* = [1\,1\,0]/2$ as its direction vector scaled in the reciprocal space, same as below) in the deformed lattice. Three other acoustic phonon modes with wave vectors of $\mathbf{q}_2^* = [1\bar{1}0]/2, \mathbf{q}_3^* = [101]/2$ and $\mathbf{q}_4^* = [10\bar{1}]/2$, respectively, have also imaginary frequencies as a result of geometrical symmetry. Analysis of the eigenvectors of the dynamical matrix indicates that the displacements of Ni and Al atoms for the four unstable modes are parallel to $\mathbf{v}_1 = [010; \bar{1}00], \mathbf{v}_2 = [010; 100], \mathbf{v}_3 = [001; \bar{1}00]$ and $\mathbf{v}_4 = [001; 100]$, respectively. These phonon modes lead to a transformation from the initial B2 structure into a low-symmetry modulated structure, and the modulation displacements **u** of each atom with respect to the homogenously strained lattice positions can be described as a sum of the four harmonic phonon modes above,

$$\mathbf{u} = \sum_{j=1}^{4} \mathbf{A}_j \exp(-i\mathbf{q}_j \cdot \mathbf{x}), \tag{26}$$
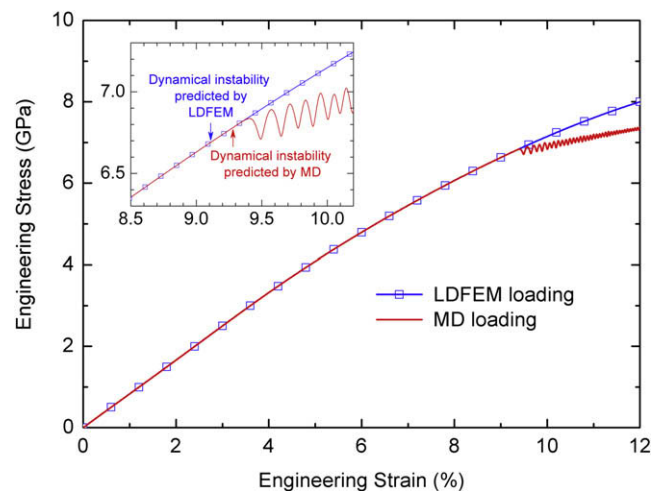
Fig. 1. Stress–strain curves of uniaxial tension along the [1 0 0] direction with LDFEM and MD simulations. The inset shows a higher magnification of the curves near the incipient instability.
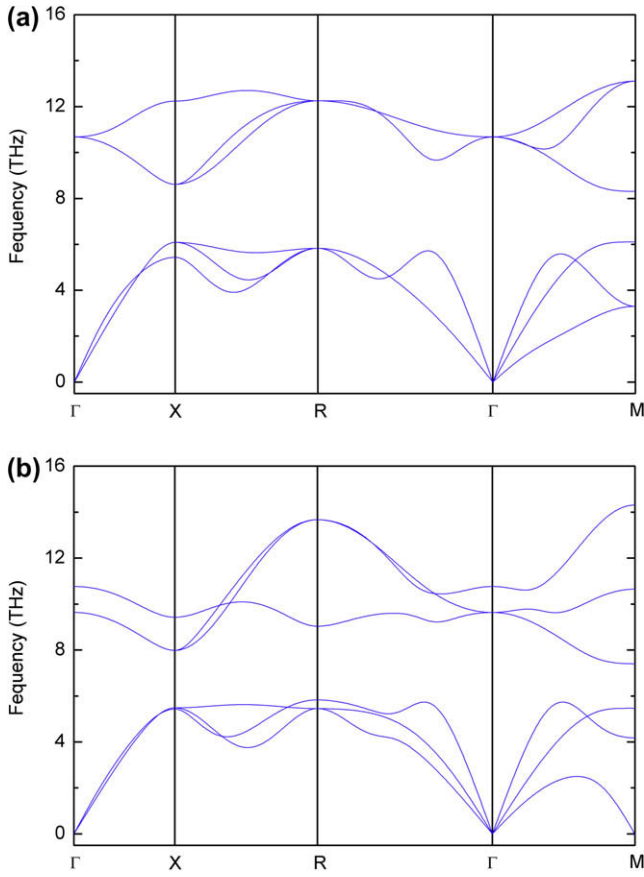
Fig. 2. Phonon spectra along high-symmetry directions of B2-NiAl for: (a) the undeformed lattice and (b) the lattice at a strain of $\varepsilon_x = 9.11\%$ under uniaxial tension along the [1 0 0] direction.

where **A** is the amplitude vector which is parallel with the corresponding eigenvector **v**. Such a three-dimensional modulated structure has been validated by the MD simulation, with a representative crystal structure at the critical strain of $\varepsilon_x = 9.28\%$ visualized by AtomEye [55], shown in Fig. 3. It results in a stress fluctuation under tension
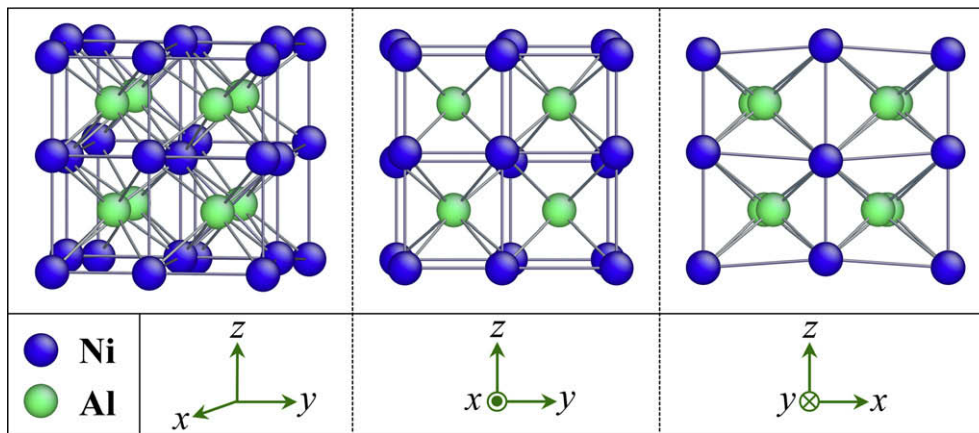
(Fig. 1) and will be reversed to a B2 structure when unloading, implying it is a metastable structure.

It is interesting that the martensitic phase transformation from an initial B2 phase into a body-centered tetragonal (bct) phase under uniaxial tension along the [1 0 0] direction seen in NiAl nanowires [56] does not occur in the present bulk NiAl. To identify the stable crystal structures under such a uniaxial tension, we analyze their enthalpy as a function of lattice parameters for specific values of uniaxial stress based on the Mishin potential. The undeformed B2 structure is set as the reference configuration. The enthalpy per primitive unit cell under applied uniaxial loading is given by [57]

$$H(b/a, c/a) = E(a, b, c, \mathbf{z}) - A_{jk}\sigma_i q_i \qquad (27)$$

where E is the formation energy per primitive unit cell, a, b and c are the lattice parameters (those with a subscript 0 are the lattice parameters of the undeformed B2 structure), σ_i is the engineering stress along the i direction, q_i is the lattice parameter in the i direction, A_{jk} is the cross section area of the undeformed primitive unit cell perpendicular to the loading direction, and $A_{jk}\sigma_i q_i$ (summation not implied) is the external work. For tension along the x axis, $i = x$, $A_{yz} = b_0 c_0$, and $q_x = a$, with σ_x being the tensile engineering stress. For each b/a and c/a pair, the lattice parameter a and the inner displacements $\mathbf{z}$ are relaxed to minimize H. Then the minimum H on the enthalpy surface with b/a and c/a as the independent variables corresponds to certain stable or metastable structure under the applied uniaxial stress. Fig. 4a and b shows the energy (equal to enthalpy at zero external loading) contour and the enthalpy contour for the critical stress $\sigma_x = 6.78$ GPa, respectively. Only one minimum can be found for both the cases with $b/a = c/a = 1.00$ and 0.88 ($H = -8.932$ and -9.964 eV), respectively. In fact, it is true for all cases from zero to the critical uniaxial tensile stress, with the only minimum corresponding to a deformed B2 structure with $b = c$ smaller than a, so the transformation from a B2 into a bct structure cannot

Fig. 3. Three-dimensional modulated structure of B2-NiAl at the critical strain of $\varepsilon_x = 9.28\%$ under uniaxial tension along the [1 0 0] direction with MD simulation. The modulation displacements of each atom with respect to the homogenously strained lattice positions are enhanced to make the modulation waves visible. For all cases, $x = [1\,0\,0]$, $y = [0\,1\,0]$ and $z = [0\,0\,1]$.
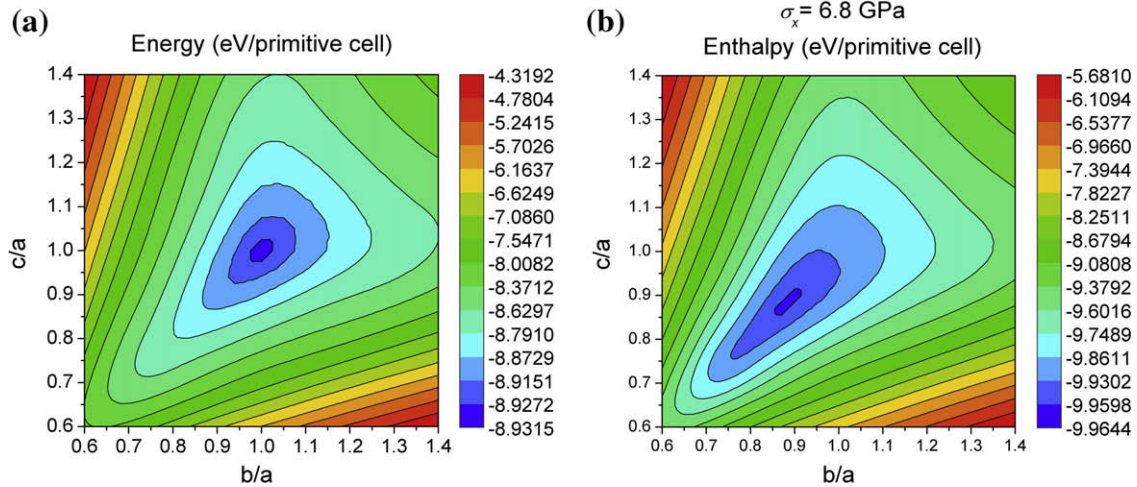
Fig. 4. Contours of: (a) energy and (b) enthalpy for uniaxial tensile stress of $\sigma_x = 6.78$ GPa along the [1 0 0] direction based on Mishin potential.

take place. In the nanowires, however, the surfaces energy plays a dominant role in inducing the martensitic phase transformation, i.e., the surfaces energy of a B2 structure is higher than that of a bct structure at a critical tensile strain, in contrast to no surfaces existing in the present bulk NiAl with PBCs, which leads to the different instability behavior for the two systems.

5.1.2. Uniaxial compression

The prediction of the stress–strain curves under uniaxial compression via the LDFEM and MD simulations is presented in Fig. 5. The cell undergoes an elastic deformation under loading from point A to B with almost the same stress–strain responses, indicating a good agreement between the two simulations. In contrast to the LDFEM's prediction of a dynamical instability at $\varepsilon_x = -13.94\%$ ($\sigma_x = -57.91$ GPa) or an elastic instability at $\varepsilon_x = -16.33\%$ ($\sigma_x = -81.82$ GPa), respectively, the MD simula-

tion confirms that a dynamical instability occurs at $\varepsilon_x = -14.09\%$ ($\sigma_x = -59.23$ GPa) corresponding to point B.

By analysis of the phonon spectrum at $\varepsilon_x = -13.94\%$ (Fig. 6), two acoustic phonon modes become unstable, with wave vectors of $\mathbf{q}_1^* = [0\,1\,1]/2$ and $\mathbf{q}_2^* = [0\,1\,\bar{1}]/2$, and eigenvectors corresponding to atom displacements of $\mathbf{v}_1 = [0\,\bar{1}\,1; 0\,\bar{1}\,1]$ and $\mathbf{v}_2 = [0\,1\,1; 0\,1\,1]$, respectively. Different from the stress fluctuation after instability under tension, the two soft phonon modes result in a stress drop from -60.09 to -58.98 GPa corresponding to point C ($\varepsilon_x = -14.43\%$). The representative crystal structures for points B and C by the MD simulation are illustrated in Fig. 7a and b, respectively. It can be seen that the cell still keeps a B2 structure at point B, but transforms into a modulated structure at point C, which also results in a stress fluctuation under further loading. It should be noted that such a modulated structure is not based on a B2 structure but on a body-centered orthorhombic (bco) structure, because the lattice parameters are obviously changed from point B to C along with a sudden volume increase of about 2%. To
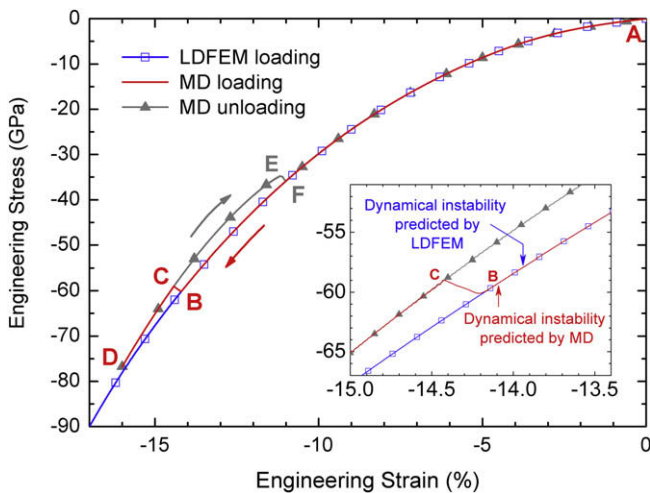
Fig. 5. Stress–strain curves of uniaxial compression along the [1 0 0] direction with LDFEM and MD simulations. The inset shows a higher magnification of the curves near the incipient instability.
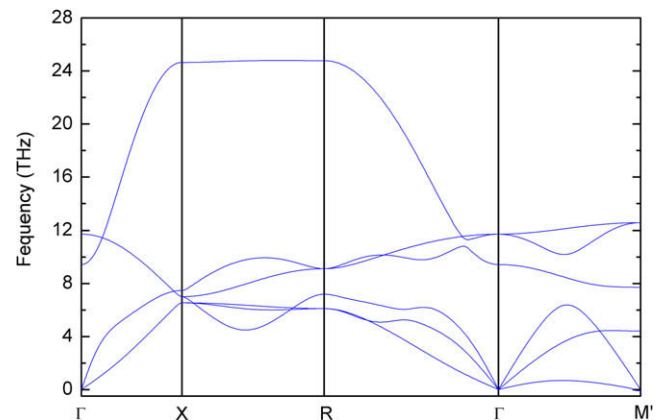
Fig. 6. Phonon spectrum along high-symmetry directions of B2-NiAl for the lattice at a strain of $\varepsilon_x = -13.94\%$ under uniaxial compression along the [1 0 0] direction. Point M' denotes the wave vector of $\mathbf{q}^* = [0\,1\,1]/2$.
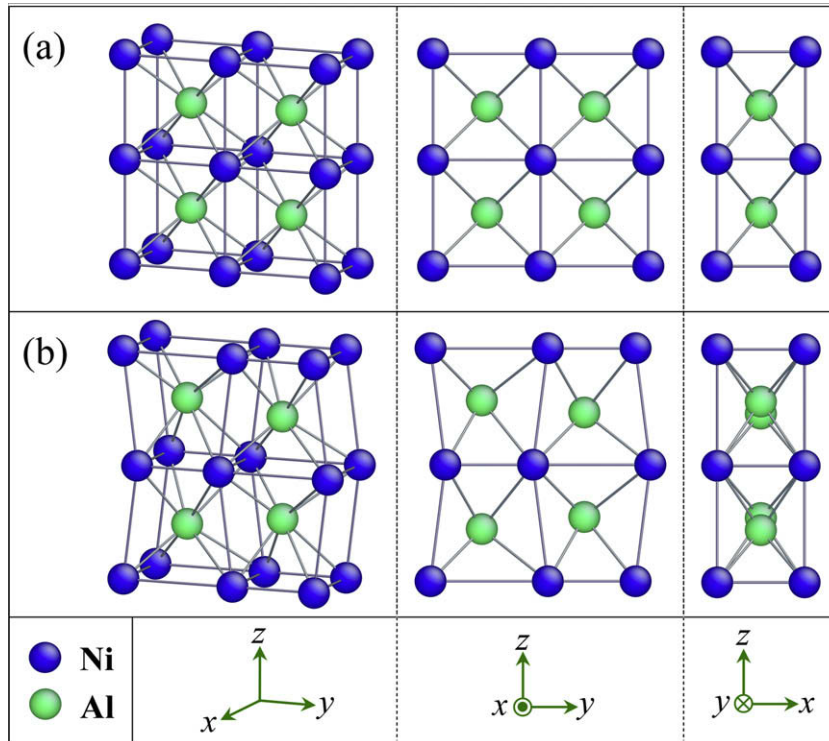
Fig. 7. Representative crystal structures at a strain of (a) $\varepsilon_x = -14.09\%$ and (b) $\varepsilon_x = -14.43\%$ corresponding to points B and C in Fig. 5, respectively, under uniaxial compression along the [1 0 0] direction with MD simulation. For all cases, $x = $ [1 0 0], $y = $ [0 1 0] and $z = $ [0 0 1].

verify such a phase transformation, we also analyze the enthalpy as a function of lattice parameters for uniaxial stress of $\sigma_x = -50$, -60, and -75 GPa, respectively. It can be seen from the enthalpy contours shown in Fig. 8 that there's only one minimum for $\sigma_x = -50$ and -60 GPa but three minima for $\sigma_x = -75$ GPa. For the former two cases, the only minimum is in the vicinity of $b/a = c/a = 1.21$ and 1.23 ($H = -2.259$ and -0.999 eV), respectively, corresponding to a B2 structure with lattice parameters slightly different from those at zero stress. For the last case, however, two minima are symmetrical with $b/a = 1.14$ and $c/a = 1.45$ (or $b/a = 1.45$ and $c/a = 1.14$), while the third one is in the vicinity of $b/a = c/a = 1.25$. The first two minima correspond to a bco structure with an enthalpy of 0.857 eV, 0.003 eV lower than that for the third corresponding to a B2 structure, implying that the bco structure is more stable. However, the formation of the ideal bco structure is not observed after instability in the MD simulation. This is because the modulated bco structure has a lower enthalpy than the ideally normal bco structure under the uniaxial compression loading with $\sigma_x \leqslant -60$ GPa. Therefore, the observed instability is a phase transformation from a B2 structure into a modulated bco structure, which is successfully predicted by LDFEM. It is notable that such a transformation can also be observed using the Voter–Chen potential [58] (not shown), but has not been reported in experiments or ab initio calculations, which are in our consideration in the further study, however.

With the progress of compression from point C, the cell undergoes an elastic deformation and keeps a modulated bco structure until it is transformed into an amorphous atomic structure at a strain of -16.73% (not shown). Unloading from any strain prior to the amorphization, e.g. point D with a strain of -16.00%, the cell is recovered elastically to point E ($\varepsilon_x = -11.19\%$, $\sigma_x = -34.75$ GPa), reversed to a B2 structure at point F ($\varepsilon_x = -11.00\%$, $\sigma_x = -35.75$ GPa) and undergoes another recovery of elastic deformation within a B2 structure till the origin point A. The different loading and unloading responses by the MD simulation give a hysteresis loop exhibiting a pseudoelastic behavior.

5.2. 2-D nanoindentation

Nanoindentation has been an effective tool for investigating the mechanical properties of materials [59]. In this section, we compare the simulations of a fully 2-D cylindrical nanoindentation of B2-NiAl crystal via both LDFEM and MD. Coordinate system is taken as $x[1\,\bar{1}\,2]$, $y[1\,1\,0]$ and $z[1\,\bar{1}\,1]$. An analytic rigid cylindrical indenter with a radius R of 100 Å and an axis along the z direction is imposed normal to the (1 1 0) surface with a size of 400×200 Å in the x–y plane. For the LDFEM simulation, 4-noded plane-strain linear rectangular elements are used, and the typical size of the elements near the indenter is about 1 Å. The model has a fixed bottom, a free top surface and two fixed sides in the x direction. There is no friction
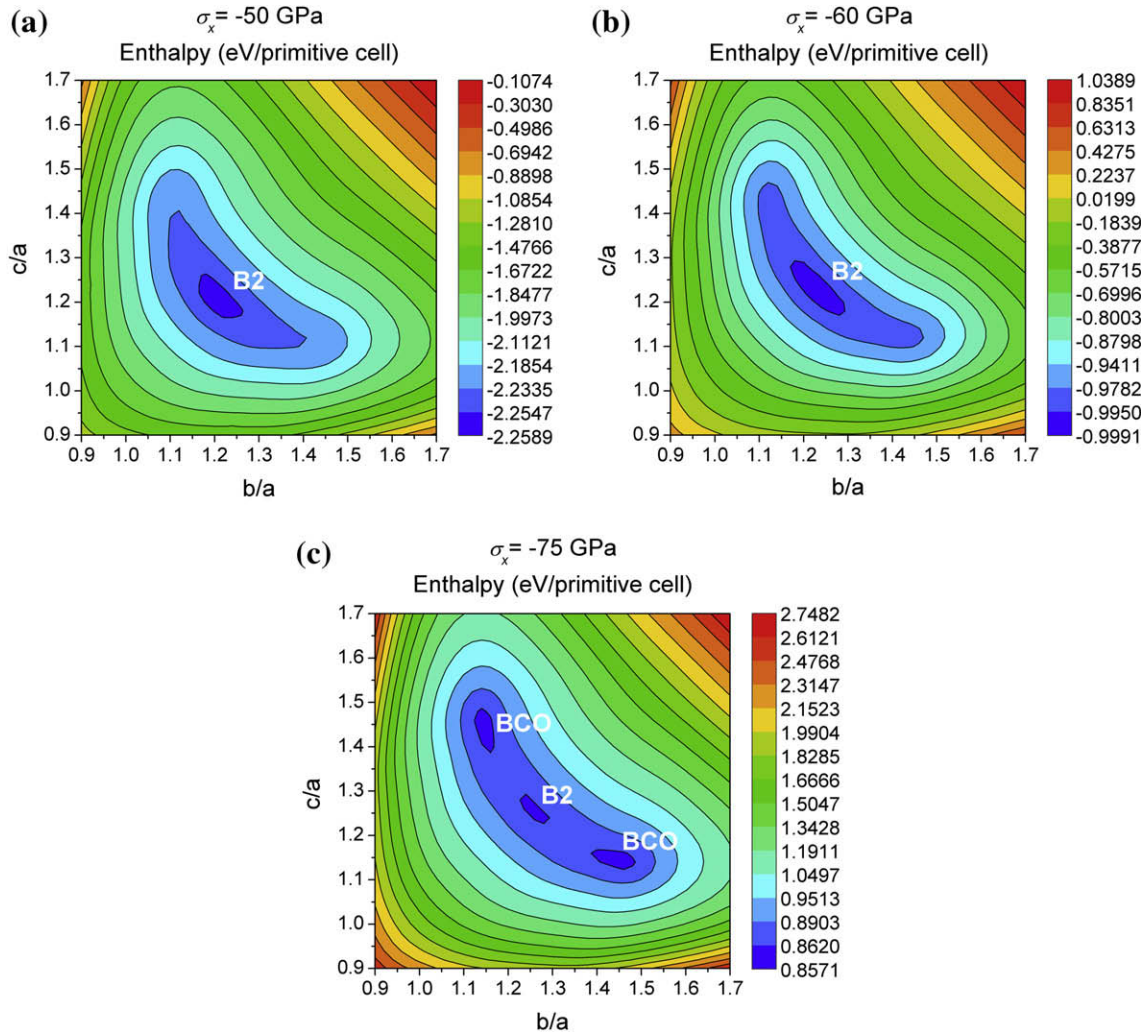
Fig. 8. Contours of enthalpy for uniaxial compression stress of: (a) $\sigma_x = -50$ GPa, (b) $\sigma_x = -60$ GPa, and (c) $\sigma_x = -75$ GPa along the [1 0 0] direction based on Mishin potential. Stable or metastable structures are denoted corresponding to the minima.

between the indenter and the top surface. The indentation proceeds in a displacement control and the indentation depth is set to 0.01 Å per step. The model for the MD simulation has a same size and boundaries in the x–y plane as those set in the LDFEM simulation, and a periodic boundary condition in the z direction. There are 9 layers of atoms of $(1\bar{1}1)$ plane along the z direction, and no displacement is allowed in this direction to be compared with the plane strain in the LDFEM simulation. The indentation is controlled in a static process with an indentation depth of 0.01 Å per step to eliminate the effect of strain rate on indentation behavior. It is achieved by introducing an external repulsive interatomic potential between the indenter and the atoms at the top surface,

$$\Psi = \begin{cases} A(r-R)^3 & \text{for } r \leqslant R \\ 0 & \text{for } r > R \end{cases}, \tag{28}$$

where r is the distance between the indenter and the atom, and $A = 50$ eV Å^{-3} is chosen empirically to control the

rigidity of the indenter in the present study. In each step, the system is thermally equilibrated at a temperature of 0.1 K using a Nosé–Hoover thermostat [60,61].

The load L versus indentation depth h responses (Fig. 9) show a good agreement between the two simulations. A dynamical instability occurs at $h = 12.38$ Å, with four soft acoustic phonon modes with wave vectors of $\mathbf{q}_1^* = [1\,0\,1]/2$, $\mathbf{q}_2^* = [1\,0\,\bar{1}]/2$, $\mathbf{q}_3^* = [0\,1\,1]/2$ and $\mathbf{q}_4^* = [0\,1\,\bar{1}]/2$ in the Brillouin zone, respectively, predicted by the soft phonon criterion. Simultaneously, the Λ criterion predicts that two dislocations with slip systems of $(0\,1\,1)\,[1\,1\,\bar{1}]$ and $(1\,0\,\bar{1})\,[1\,1\,1]$, respectively, are equally likely to be activated at $h = 13.59$ Å. The two criteria predict the same instability material point (element), which is 36.05 and 37.09 Å below the initial top surface along the central y axis at each respective critical indentation depth.

Even though the indentation deformation is limited to 2-D, the predicted instability products may have 3-D configurations. To verify the 3-D instability predictions by the criteria, each configuration of the model per indentation
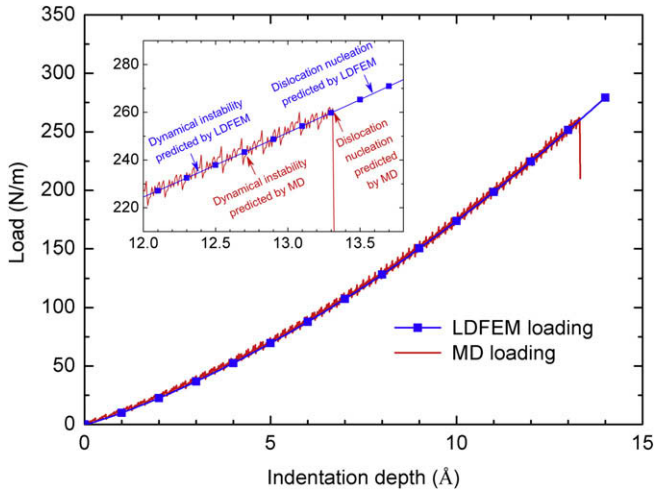
Fig. 9. Load versus indentation depth curves of the 2-D nanoindentation with LDFEM and MD simulations. The inset shows a higher magnification of the curves near the incipient instability.

depth of 0.01 Å near the incipient instability in the MD simulation is saved, and then post-processed to get an equilibrated state by relaxing the displacements of atoms in all the three directions. It is found that a modulated structure and a dislocation dipole are nucleated at $h = 12.71$ and 13.32 Å, respectively, a little higher and lower than each respective critical indentation depth corresponding to the dynamical and elastic instability predicted by the two instability criteria in the LDFEM simulation. The positions of the two nucleation sites are 37.78 and 40.16 Å below the initial top surface along the central y axis, respectively, agreeing well with the LDFEM simulation results. The equilibrated configurations of the model at the two critical indentation depths above are shown in

Figs. 10 and 11, respectively. It can be seen that a modulated structure develops firstly in a local region surrounded by stable lattices during relaxation (Fig. 10). The surrounding stable lattices acting as a "firewall" isolates the unstable region so that the load drop cannot be seen in the L–h curve. After the indentation depth reaches a critical value, the unstable region breaks through the "firewall" in relaxation and leads to a nucleation of a dislocation dipole (Fig. 11). The asynchrony of the two critical depths shows that the dynamical instability does not necessarily mean immediate structural collapse [62], e.g. dislocation nucleation. It is notable that the critical indentation depth of 13.32 Å in the MD simulation is ahead of 13.59 Å corresponding to an elastic instability, implying that the nucleation of the dislocation dipole is still a product of dynamical instability. With the development of the indentation depth, the dislocation dipole then splits under full relaxation, with the lower dislocation migrating into the inner of the crystal and the upper slipping to the top surface along the slip plane of (0 1 1), which results in a load drop. Both members of the dipole are mixed dislocations in nature, with slip directions of [1 1 $\bar{1}$] and [$\bar{1}$ $\bar{1}$ 1], respectively, and the same direction of dislocation line along the z[1 $\bar{1}$ 1] direction. This first nucleated dipole suppresses the nucleation of the other equivalent one with a slip plane of (1 0 $\bar{1}$), which is also possible to be activated predicted by the instability criterion.

The von Mises stress distributions calculated by LDFEM and MD at $h = 12.70$ Å just before the incipient instability are compared, shown in Fig. 12a and b, respectively. Note that the Cauchy stress by Eq. (21) for both the methods is not defined for a single atom but a primitive unit cell. In the LDFEM simulation, the stress at each material point is calculated based on the local deformation
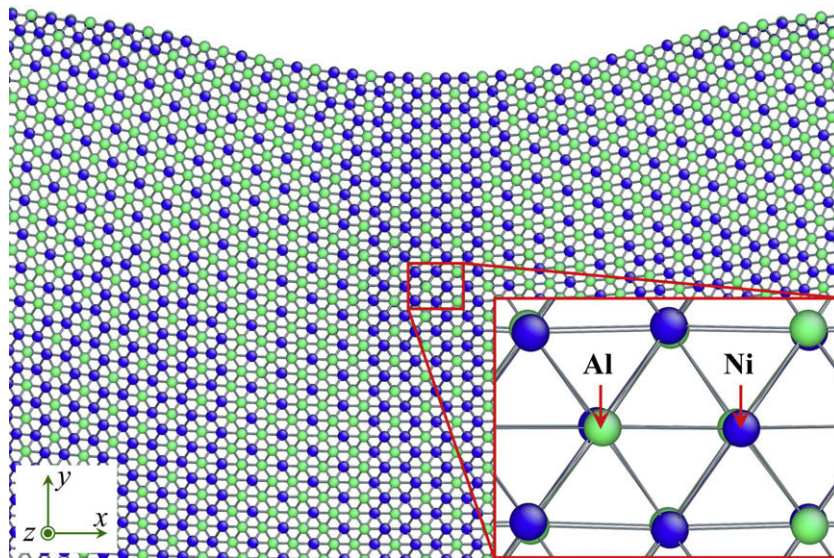
Fig. 10. Equilibrated configuration by full relaxation of the 2-D nanoindentation system at an indentation depth of 12.71 Å with MD simulation. The inset shows a higher magnification of the region where a modulated structure appears incipiently. The coordinate system is taken as $x = [1 \bar{1} \bar{2}]$, $y = [1 1 0]$ and $z = [1 \bar{1} 1]$.
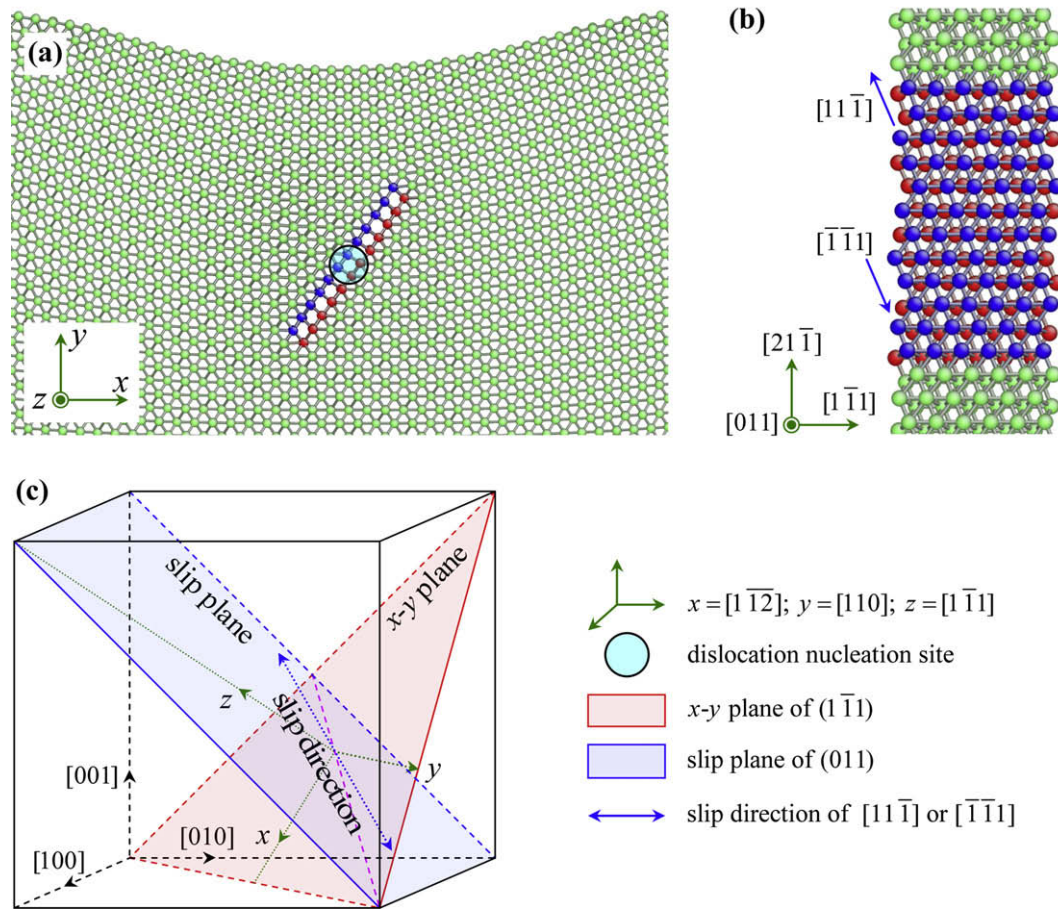
Fig. 11. Atomic structure of the dislocation dipole by full relaxation of the 2-D nanoindentation system at an indentation depth of 13.32 Å with MD simulation: (a) view along the $z[1\bar{1}1]$ direction; (b) view along the normal direction of the slip plane of (0 1 1), with the atoms below and above the two adjacent slip planes near the incipient dislocation nucleation site being removed; (c) illustration of the slip system of the dislocation dipole. Red and blue atoms are those on the two adjacent slip planes.

gradient. While in the MD simulation, it is needed to classify each atom into respective primitive unit cell firstly, and then calculate the Cauchy stress by substituting the actual coordinates of the neighboring atoms into Eqs. (16) and (21). Both the simulations give the maximum von Mises stress of about 34 GPa. The good agreement of the von Mises stress distributions obtained by the two methods further validates that LDFEM simulation is faithful to the underlying atomistic model.

6. Conclusions and discussions

We have proposed a constitutive relation of LDFEM for complex crystals incorporating the crystalline anisotropy and nonlinear elastic effects within the hyperelasticity framework. In this method, the CB hypothesis has been employed to link the macroscopic continuum elastic deformation to microscopic atoms movements, and the inner displacement has been elaborately considered, as it differentiates the constitutive model between monatomic and complex crystals. The explicit expressions for the stress and elastic tensor have been derived based on the EAM potential for complex Bravais lattices, and simultaneously, two energy-based lattice instability criteria to be embedded into LDFEM for predicting homogenous lattice instability in a perfect crystal have been critically reviewed.

LDFEM and MD simulations of uniaxial loadings of single-crystal B2-NiAl with 3-D PBCs along the [1 0 0] direction have been performed, and homogeneous lattice instabilities by the two instability criteria have been predicted. The results from both the methods have been carefully compared. The good agreement of the stress–strain responses and the predicted instability behaviors by the two methods validates the proposed LDFEM's capability to perform simulations at atomic scale. The MD simulations confirm that a dynamical instability occurs incipiently under both the uniaxial tension and compression loadings, though with different products: a modulated structure and a new phase, respectively. The absolute value of stress required for the incipient instability under tension is 6.78 GPa, much lower than that of 59.23 GPa under compression, showing the asymmetry of tension and compression of B2-NiAl along the [1 0 0] direction.

The proposed method is further validated by comparing the results of a fully 2-D cylindrical nanoindentation of NiAl with the LDFEM and MD simulations. Both the accordance
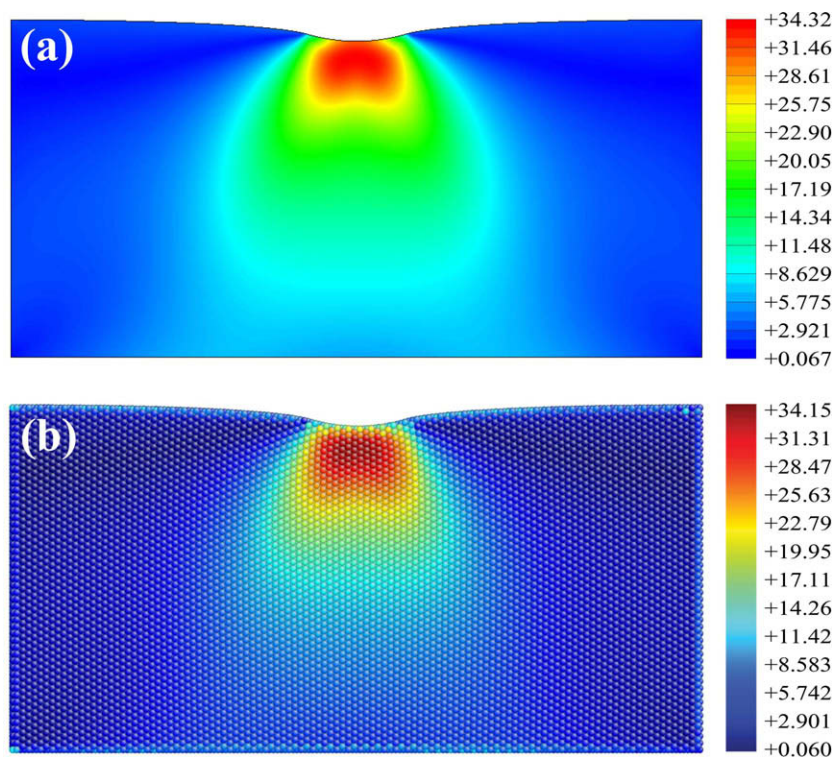
Fig. 12. Contours of von Mises stress (in GPa) at an indentation depth of 12.70 Å with: (a) LDFEM and (b) MD simulations.

of the indentation load–depth responses and the von Mises stress distributions indicate that LDFEM is able to deal with complex loading problems. The two critical indentation depths, corresponding to a dynamical instability and a dislocation nucleation predicted by the two criteria in the LDFEM simulation, respectively, give lower and upper bounds for those in the MD simulation. It can be explained as follows: a threshold volume of region is required to accommodate unstable waves to transmit, so the occurrence of an actual homogenous dynamical instability, e.g. formation of a modulated structure, lags behind the ideal criterion's prediction; only after the region grows up to a critical volume can the unstable waves break through the "firewall" which isolates the unstable regions from stable ones, transmit to the entire system and then lead to dislocation nucleation. Such a nucleation occurs before the elastic instability as a result of its short-wavelength-instability nature. This scenario is different from the study by Dmitriev et al. [62], in which the soft phonon criterion predicts that the crystal would become unstable firstly in the long wavelength limit corresponding to an elastic instability, though no dislocation is nucleated actually until unstable waves with relatively shorter wavelength appear.

IPFEM's significant computational efficiency in dealing with large-length-scale system without losing atomic resolution has been exhibited in the previous studies [34,36–39]. In fact, it is very suitable to investigate the mechanical properties such as theoretical strength and hardness of materials at large length scales. Besides inheriting such a prominent feature of IPFEM, the presently developed LDFEM greatly broadens the investigated materials once the structure and the interatomic potential of the material are given. Furthermore, it is quite promising for LDFEM to couple with other atomistic simulation methods to realize studies of complicated mechanical response of materials with experimentally length/time scales. Simultaneously, many extensions are under development to further broaden the LDFEM's applicability. For instance, the presence of defects such as free surfaces and pre-existing dislocation, finite temperature and strain-rate dependence of mechanical responses may be included in the future. Such extensions may help LDFEM become a versatile multiscale simulation method.

Appendix A. Derivatives of the strain energy density

The first and second derivatives of the EAM-based strain energy density W with respect to the Green strain $\mathbf{E}$ or/and the inner displacements $\mathbf{z}$, are given by

$$\frac{\partial W}{\partial E_{ij}} = \frac{1}{\Omega_0} \sum_\alpha^\wedge \left\{ \sum_{\beta \neq \alpha} \left[\left(\frac{1}{2} \frac{\partial V^{\alpha\beta}}{\partial r^{\alpha\beta}} + \frac{\partial U^\alpha}{\partial \bar\rho^\alpha} \frac{\partial \rho^\beta}{\partial r^{\alpha\beta}} \right) \frac{\partial r^{\alpha\beta}}{\partial E_{ij}} \right] \right\}, \quad (A.1)$$

$$\frac{\partial^2 W}{\partial E_{ij} \partial E_{kl}} = \frac{1}{\Omega_0} \sum_\alpha^\wedge \left\{ \sum_{\beta \neq \alpha} \left[\left(\frac{1}{2} \frac{\partial^2 V^{\alpha\beta}}{(\partial r^{\alpha\beta})^2} + \frac{\partial U^\alpha}{\partial \bar\rho^\alpha} \frac{\partial^2 \rho^\beta}{(\partial r^{\alpha\beta})^2} \right) \right. \right.$$
$$\times \frac{\partial r^{\alpha\beta}}{\partial E_{ij}} \frac{\partial r^{\alpha\beta}}{\partial E_{kl}} + \left(\frac{1}{2} \frac{\partial V^{\alpha\beta}}{\partial r^{\alpha\beta}} + \frac{\partial U^\alpha}{\partial \bar\rho^\alpha} \frac{\partial \rho^\beta}{\partial r^{\alpha\beta}} \right) \frac{\partial^2 r^{\alpha\beta}}{\partial E_{ij} \partial E_{kl}} \right]$$
$$\left. + \frac{\partial^2 U^\alpha}{(\partial \bar\rho^\alpha)^2} \sum_{\beta \neq \alpha} \left(\frac{\partial \rho^\beta}{\partial r^{\alpha\beta}} \frac{\partial r^{\alpha\beta}}{\partial E_{ij}} \right) \sum_{\beta \neq \alpha} \left(\frac{\partial \rho^\beta}{\partial r^{\alpha\beta}} \frac{\partial r^{\alpha\beta}}{\partial E_{kl}} \right) \right\}, \quad (A.2)$$

$$\frac{\partial^2 W}{\partial E_{ij} \partial z_n^q} = \frac{1}{\Omega_0} \sum_\alpha^\wedge \left\{ \sum_{\beta \neq \alpha} \left[\left(\frac{1}{2} \frac{\partial^2 V^{\alpha\beta}}{(\partial r^{\alpha\beta})^2} + \frac{\partial U^\alpha}{\partial \bar\rho^\alpha} \frac{\partial^2 \rho^\beta}{(\partial r^{\alpha\beta})^2} \right) \frac{\partial r^{\alpha\beta}}{\partial E_{ij}} \right) \right. \right.$$
$$\times \frac{\partial r^{\alpha\beta}}{\partial z_n^q} + \left(\frac{1}{2} \frac{\partial V^{\alpha\beta}}{\partial r^{\alpha\beta}} + \frac{\partial U^\alpha}{\partial \bar\rho^\alpha} \frac{\partial \rho^\beta}{\partial r^{\alpha\beta}} \right) \frac{\partial^2 r^{\alpha\beta}}{\partial E_{ij} \partial z_n^q} \right]$$
$$\left. + \frac{\partial^2 U^\alpha}{(\partial \bar\rho^\alpha)^2} \sum_{\beta \neq \alpha} \left(\frac{\partial \rho^\beta}{\partial r^{\alpha\beta}} \frac{\partial r^{\alpha\beta}}{\partial E_{ij}} \right) \sum_{\beta \neq \alpha} \left(\frac{\partial \rho^\beta}{\partial r^{\alpha\beta}} \frac{\partial r^{\alpha\beta}}{\partial z_n^q} \right) \right\}, \quad (A.3)$$

$$\frac{\partial^2 W}{\partial z_m^p \partial z_n^q} = \frac{1}{\Omega_0} \sum_\alpha^\wedge \left\{ \sum_{\beta \neq \alpha} \left[\left(\frac{1}{2} \frac{\partial^2 V^{\alpha\beta}}{(\partial r^{\alpha\beta})^2} + \frac{\partial U^\alpha}{\partial \bar\rho^\alpha} \frac{\partial^2 \rho^\beta}{(\partial r^{\alpha\beta})^2} \right) \right. \right.$$
$$\times \frac{\partial r^{\alpha\beta}}{\partial z_m^p} \frac{\partial r^{\alpha\beta}}{\partial z_n^q} + \left(\frac{1}{2} \frac{\partial V^{\alpha\beta}}{\partial r^{\alpha\beta}} + \frac{\partial U^\alpha}{\partial \bar\rho^\alpha} \frac{\partial \rho^\beta}{\partial r^{\alpha\beta}} \right) \frac{\partial^2 r^{\alpha\beta}}{\partial z_m^p \partial z_n^q} \right]$$
$$\left. + \frac{\partial^2 U^\alpha}{(\partial \bar\rho^\alpha)^2} \sum_{\beta \neq \alpha} \left(\frac{\partial \rho^\beta}{\partial r^{\alpha\beta}} \frac{\partial r^{\alpha\beta}}{\partial z_m^p} \right) \sum_{\beta \neq \alpha} \left(\frac{\partial \rho^\beta}{\partial r^{\alpha\beta}} \frac{\partial r^{\alpha\beta}}{\partial z_n^q} \right) \right\}. \quad (A.4)$$

Appendix B. Derivatives of the distance between two atoms

The first and second derivatives of $r^{\alpha\beta}$, the distance between atoms α and β, with respect to the Green strain **E** or/and the inner displacements **z**, are given by

$$\frac{\partial r^{\alpha\beta}}{\partial E_{ij}} = \frac{R_i^{\alpha\beta} R_j^{\alpha\beta}}{r^{\alpha\beta}}, \quad (B.1)$$

$$\frac{\partial r^{\alpha\beta}}{\partial z_m^p} = \frac{r_m^{\alpha\beta}}{r^{\alpha\beta}} (\delta_{bp} - \delta_{ap}), \quad (B.2)$$

$$\frac{\partial^2 r^{\alpha\beta}}{\partial E_{ij} \partial E_{kl}} = -\frac{R_i^{\alpha\beta} R_j^{\alpha\beta} R_k^{\alpha\beta} R_l^{\alpha\beta}}{(r^{\alpha\beta})^3}, \quad (B.3)$$

$$\frac{\partial^2 r^{\alpha\beta}}{\partial E_{ij} \partial z_m^p} = \left[\frac{R_i^{\alpha\beta} \delta_{jm} + R_j^{\alpha\beta} \delta_{im}}{r^{\alpha\beta}} - \frac{R_i^{\alpha\beta} R_j^{\alpha\beta} r_m^{\alpha\beta}}{(r^{\alpha\beta})^3} \right] (\delta_{bp} - \delta_{ap}), \quad (B.4)$$

$$\frac{\partial^2 r^{\alpha\beta}}{\partial z_m^p \partial z_n^q} = \left[\frac{\delta_{mn}}{r^{\alpha\beta}} - \frac{r_m^{\alpha\beta} r_n^{\alpha\beta}}{(r^{\alpha\beta})^3} \right] (\delta_{bp} - \delta_{ap})(\delta_{bq} - \delta_{aq}). \quad (B.5)$$

Appendix C. Derivative of the total potential energy

With restriction to the EAM potential, the total potential energy $\bar\Psi$, determined by summation of the interatomic potential over all atoms in the system, is given by

$$\bar\Psi = \sum_\alpha \sum_{\beta \neq \alpha} \frac{1}{2} V^{\alpha\beta}(r^{\alpha\beta}) + \sum_\alpha U^\alpha(\bar\rho^\alpha). \quad (C.1)$$

The second derivative of $\bar\Psi$ with respect to the coordinates of two different atoms α and β is given by

$$\frac{\partial^2 \bar\Psi}{\partial x_i^\alpha \partial x_j^\beta} = -\left[\frac{\partial^2 V^{\alpha\beta}}{(\partial r^{\alpha\beta})^2} + \frac{\partial U^\alpha}{\partial \bar\rho^\alpha} \frac{\partial^2 \rho^\beta}{(\partial r^{\alpha\beta})^2} + \frac{\partial U^\beta}{\partial \bar\rho^\beta} \frac{\partial^2 \rho^\alpha}{(\partial r^{\alpha\beta})^2} \right] \frac{r_i^{\alpha\beta} r_j^{\alpha\beta}}{(r^{\alpha\beta})^2}$$
$$- \left(\frac{\partial V^{\alpha\beta}}{\partial r^{\alpha\beta}} + \frac{\partial U^\alpha}{\partial \bar\rho^\alpha} \frac{\partial \rho^\beta}{\partial r^{\alpha\beta}} + \frac{\partial U^\beta}{\partial \bar\rho^\beta} \frac{\partial \rho^\alpha}{\partial r^{\alpha\beta}} \right) \frac{(r^{\alpha\beta})^2 \delta_{ij} - r_i^{\alpha\beta} r_j^{\alpha\beta}}{(r^{\alpha\beta})^3}$$
$$- \frac{\partial^2 U^\beta}{(\partial \bar\rho^\beta)^2} \frac{\partial \rho^\alpha}{\partial r^{\alpha\beta}} \frac{r_i^{\alpha\beta}}{r^{\alpha\beta}} \sum_{\gamma \neq \beta} \left(\frac{\partial \rho^\gamma}{\partial r^{\gamma\beta}} \frac{r_j^{\gamma\beta}}{r^{\gamma\beta}} \right) - \frac{\partial^2 U^\alpha}{(\partial \bar\rho^\alpha)^2}$$
$$\times \frac{\partial \rho^\beta}{\partial r^{\alpha\beta}} \frac{r_j^{\alpha\beta}}{r^{\alpha\beta}} \sum_{\gamma \neq \alpha} \left(\frac{\partial \rho^\gamma}{\partial r^{\alpha\gamma}} \frac{r_i^{\alpha\gamma}}{r^{\alpha\gamma}} \right)$$
$$- \sum_{\gamma \neq \alpha, \beta} \left[\frac{\partial^2 U^\gamma}{(\partial \bar\rho^\gamma)^2} \frac{\partial \rho^\alpha}{\partial r^{\alpha\gamma}} \frac{\partial \rho^\beta}{\partial r^{\gamma\beta}} \frac{r_i^{\alpha\gamma}}{r^{\alpha\gamma}} \frac{r_j^{\gamma\beta}}{r^{\gamma\beta}} \right]. \quad (C.2)$$

References

[1] Xiao SP, Yang WX. Int J Comput Methods 2005;2:293.
[2] Tadmor EB, Ortiz M, Phillips R. Philos Mag A 1996;73:1529.
[3] Miller RE, Tadmor EB. J Comput-Aided Mater Des 2002;9:203.
[4] Tadmor EB, Miller RE, Phillips R, Ortiz M. J Mater Res 1999;14:2233.
[5] Shenoy VB, Miller RE, Tadmor EB, Rodney D, Phillips R, Ortiz M. J Mech Phys Solids 1999;47:611.
[6] Knap J, Ortiz M. Phys Rev Lett 2003;90:226102.
[7] Shan DB, Yuan L, Guo B. Mater Sci Eng A 2005;412:264.
[8] Iglesias RA, Leiva EPM. Acta Mater 2006;54:2655.
[9] Jin J, Shevlin SA, Guo ZX. Acta Mater 2008;56:4358.
[10] Miller RE, Rodney D. J Mech Phys Solids 2008;56:1203.
[11] Dupont V, Sansoz F. Acta Mater 2008;56:6013.
[12] Miller RE, Tadmor EB, Phillips R, Ortiz M. Model Simul Mater Sci Eng 1998;6:607.
[13] Miller RE, Ortiz M, Phillips R, Shenoy VB, Tadmor EB. Eng Fract Mech 1998;61:427.
[14] Hai S, Tadmor EB. Acta Mater 2003;51:117.
[15] Shenoy VB, Miller RE, Tadmor EB, Phillips R, Ortiz M. Phys Rev Lett 1998;80:742.
[16] Sansoz F, Molinari JF. Scripta Mater 2004;50:1283.
[17] Sansoz F, Molinari JF. Acta Mater 2005;53:1931.
[18] Warner DH, Sansoz F, Molinari JF. Int J Plast 2006;22:754.
[19] Tadmor EB, Phillips R, Ortiz M. Langmuir 1996;12:4529.
[20] Shenoy VB, Phillips R, Tadmor EB. J Mech Phys Solids 2000;48:649.
[21] Abraham FF, Broughton JQ, Bernstein N, Kaxiras E. Europhys Lett 1998;44:783.
[22] Rudd RE, Broughton JQ. Phys Rev B 1998;58:R5893.
[23] Shilkrot LE, Miller RE, Curtin WA. Phys Rev Lett 2002;89:025501.
[24] Belytschko T, Xiao SP. Int J Multiscale Comput Eng 2003;1:115.
[25] Tadmor EB, Smith GS, Bernstein N, Kaxiras E. Phys Rev B 1999;59:235.
[26] Smith GS, Tadmor EB, Kaxiras E. Phys Rev Lett 2000;84:1260.
[27] Smith GS, Tadmor EB, Bernstein N, Kaxiras E. Acta Mater 2001;49:4089.
[28] Tadmor EB, Waghmare UV, Smith GS, Kaxiras E. Acta Mater 2002;50:2989.
[29] Fago M, Hayes RL, Carter EA, Ortiz M. Phys Rev B 2004;70:100102.
[30] Hayes RL, Ho G, Ortiz M, Carter EA. Philos Mag 2006;86:2343.
[31] Tang Z, Zhao H, Li G, Aluru NR. Phys Rev B 2006;74:064110.
[32] Johnson HT, Phillips R, Freund LB. Mater Res Soc Symp Proc 1999;538:479.
[33] Zhang P, Huang Y, Geubelle PH, Klein PA, Hwang KC. Int J Solids Struct 2002;39:3893.

[34] Li J, Van Vliet KJ, Zhu T, Yip S, Suresh S. Nature 2002;418:307.
[35] Ericksen JL. In: Gurtin ME, editor. Phase transformations and material instabilities in solids. New York: Academic Press; 1984. p. 61.
[36] Van Vliet KJ, Li J, Zhu T, Yip S, Suresh S. Phys Rev B 2003;67:104105.
[37] Zhu T, Li J, Van Vliet KJ, Ogata S, Yip S, Suresh S. J Mech Phys Solids 2004;52:691.
[38] Zhong Y, Zhu T. Comput Meth Appl Mech Eng 2008;197:3174.
[39] Liu XH, Gu JF, Shen Y, Chen CF. Scripta Mater 2008;58:564.
[40] Clatterbuck DM, Krenn CR, Cohen ML, Morris JW. Phys Rev Lett 2003;91:135501.
[41] Daw MS, Baskes MI. Phys Rev B 1984;29:6443.
[42] Belytschko T, Liu WK, Moran B. Nonlinear finite elements for continua and structures. Chichester: Wiley; 2004.
[43] Hibbitt HD, Karlsson GI, Sorensen EP. ABAQUS, Reference manuals, V6.5, 2004.
[44] Hill R. J Mech Phys Solids 1962;10:1.
[45] Hill R. Math Proc Camb Philos Soc 1975;77:225.
[46] Rice JR. In: Koiter WT, editor. Theoretical and applied mechanics. Amsterdam; 1976. p. 207.
[47] Li J, Zhu T, Yip S, Van Vliet KJ, Suresh S. Mater Sci Eng A 2004;365:25.
[48] Li J, Ngan AHW, Gumbsch P. Acta Mater 2003;51:5711.
[49] Liu F, Ming P, Li J. Phys Rev B 2007;76:064120.
[50] Born M, Huang K. Dynamical theory of crystal lattices. Oxford: Clarendon Press; 1956.
[51] Plimpton S. J Comput Phys 1995;117:1.
[52] <http://lammps.sandia.gov>.
[53] Mishin Y, Mehl MJ, Papaconstantopoulos DA. Phys Rev B 2002;65:224114.
[54] Melchionna S, Ciccotti G, Holian BL. Mol Phys 1993;78:533.
[55] Li J. Model Simul Mater Sci Eng 2003;11:173.
[56] Park HS. Nano Lett 2006;6:958.
[57] Kulkarni AJ, Zhou M, Sarasamak K, Limpijumnong S. Phys Rev Lett 2006;97:105502.
[58] Voter AF, Chen SP. Mater Res Soc Symp Proc 1987;82:175.
[59] Gouldstone A, Chollacoop N, Dao M, Li J, Minor AM, Shen YL. Acta Mater 2007;55:4015.
[60] Nosé S. J Chem Phys 1984;81:511.
[61] Hoover WG. Phys Rev A 1985;31:1695.
[62] Dmitriev SV, Li J, Yoshikawa N, Shibutani Y. Philos Mag 2005;85:2177.